

Particle acceleration in neutron star ultra-strong electromagnetic fields

Ivan Tomczak^{1†} and Jérôme Pétri^{1‡}

¹Université de Strasbourg, CNRS, Observatoire astronomique de Strasbourg, UMR 7550, F-67000, France.

(Received xx; revised xx; accepted xx)

In this paper, we discuss the results of a new particle pusher in realistic ultra-strong electromagnetic fields as those encountered around rotating neutron stars. After presenting results of this algorithm in simple fields and comparing them to expected exact analytical solutions, we present new simulations for a rotating magnetic dipole in vacuum for a millisecond pulsar by using Deutsch solution. Particles are injected within the magnetosphere, neglecting radiation reaction, interaction among them and their feedback on the fields. Our simulations are therefore not yet fully self-consistent because Maxwell equations are not solved according to the current produced by these particles. The code highlights the symmetrical behaviour of particles of opposite charge to mass ratio q/m with respect to the north and south hemispheres. The relativistic Lorentz factor of the accelerated particles is proportional to this ratio q/m : protons reach up to $\gamma_p \simeq 10^{10.7}$, whereas electrons reach up to $\gamma_e \simeq 10^{14}$.

Our simulations show that particles could be either captured by the neutron star, trapped around it, or ejected far from it, well outside the light-cylinder. Actually, for a given charge to mass ratio, particles follow similar trajectories. These particle orbits show some depleted directions, especially at high magnetic inclination with respect to the rotation axis for positive charges and at low inclination for negative charges because of symmetry. Other directions are preferred and loaded with a high density of particles, some directions concentrating the highest or lowest acceleration efficiencies.

1. Introduction

For massive enough stars, nuclear fusion is able to produce elements heavier than carbon and oxygen up to the production of the most stable nucleus, iron ^{56}Fe . At this point the core of the star collapses and the outer layers fall onto the core, triggering a supernova explosion leaving behind a compact remnant which can either be a black hole or a neutron star. In this paper, we focus on strongly magnetized and fast rotating neutron stars. These compact objects are believed to be among the most efficient accelerators in the universe, producing ultra-relativistic particles (electrons, positrons, protons and maybe ions). In its simplest description, a neutron star is described thanks to only a few parameters, namely

- the inclination angle or obliquity χ which represent the angle between the rotation axis and magnetic axis.
- the angular speed Ω which defines the light cylinder radius $r_L = c/\Omega$, the distance at which an object in Ω -rotation with the star reaches the speed of light c .
- the radius of the neutron star R .

† Email address for correspondence: ivan.tomczak@astro.unistra.fr

‡ Email address for correspondence: jerome.petri@astro.unistra.fr

- the magnetic field strength B at the surface on the equator.

The extreme magnetic fields of these remnant stars range from $B \simeq 10^5$ T to $B \simeq 10^{10}$ T, which coupled with the angular speed between $\Omega \simeq 1000$ rad.s⁻¹ and $\Omega \simeq 0.1$ rad.s⁻¹ generates an intense electric field E , of the order $\Omega B R \approx 10^{12}$ V/m, accelerating particles around the neutron star to ultra-relativistic Lorentz factors. In our applications, the neutron star mass M is irrelevant because the gravitational force exerted on charged particles F_g is negligible compared to the Lorentz force F_L . Indeed, both forces have a typical intensity of $F_g = G \frac{M m_p}{R^2} \simeq 3.17 \times 10^{-15}$ N for a proton at the surface of the neutron star compared to $F_L = q E = q \Omega R B \simeq 5.01 \times 10^{-7}$ N. The ratio of these forces is

$$\frac{F_g}{F_L} = \frac{G M m_p}{R^2 q E} = 6.33 \times 10^{-9} \ll 1$$

so the electromagnetic force is $\sim 10^8$ times stronger than the gravitational force for protons and a factor m_p/m_e larger for electrons and positrons.

Most numerical simulations of neutron star magnetospheres use the Boris (1970) algorithm or better the Vay (2008) algorithm. However these algorithms are not well suited for ultra-strong electromagnetic fields, forcing some authors to lower the true field strengths to unrealistically low values in the simulations. Although a scaling is sometimes applied to get more realistic results, such scaling cannot be straightforwardly extrapolated for instance when radiation reaction is included because of the non linearities introduced by radiative feedback (Vranic *et al.* 2016). Moreover, Lorentz factors reached by the particles near pulsars hardly exceed $\gamma = 10^4$ with those algorithms, see for instance Brambilla *et al.* (2018), Philippov & Spitkovsky (2014), Guépin *et al.* (2019) and Kalapotharakos *et al.* (2018).

Several attempts have been proposed to faithfully follow particles in relativistic regimes, trying to conserve energy and momentum. In this spirit Zenitani & Umeda (2018) improved the Boris (1970) particle pusher by computing the exact analytical rotation in the magnetic field and getting better accuracy. The Boris algorithm is however popular because of its simplicity and accuracy. Moreover its stability property takes its root in its phase space volume preserving properties as discussed by Qin *et al.* (2013). Umeda (2018) also improved the Boris algorithm by employing a three stage step. Relativistic simulations are even more stringent about numerical error accumulation and volume preserving schemes are highly recommended as pointed out by Zhang *et al.* (2015).

Efficient particle pushers in ultra-strong electromagnetic fields are fundamental to simulate the neutron star electrodynamics. For a comprehensive comparison of relativistic particle integrators, see the extensive work done by Ripperda *et al.* (2018). They carefully compared the merit of the standard Boris algorithm Boris (1970), the Vay (2008) implicit scheme in space velocity, the Higuera & Cary (2017) second order method and the implicit midpoint method described in Lapenta & Markidis (2011). This leapfrog scheme already appeared in Verboncoeur (2005). A fully implicit update in space and velocity parameters for relativistic particle integrators relying on Vay (2008) velocity advance has been explored by Pétri (2017). There it has been shown that catching properly and accurately the simple electric drift motion in an ultra relativistic regime remains extremely difficult to achieve. Unfortunately, neutron star magnetospheres are common places for such relativistic drift velocities. It is therefore compulsory to design efficient and accurate numerical schemes to faithfully follow these trajectories. It represents a crucial step towards realistic particle acceleration and radiation in ultra-strong electromagnetic fields. Some tests of particle acceleration in a plane electromagnetic wave using standard

pushers and reported by Arefiev *et al.* (2015) showed severe limitations in the accuracy already for modest field strengths with strength parameter $a \approx 20$ (see eq. 1.1).

The limitation arises from the huge span in time scales, from the gyroperiod frequency $\omega_B = qB/m$ to the stellar rotation frequency Ω and synthesised by the strength parameter

$$a = \frac{\omega_B}{\Omega} = \frac{qB}{m\Omega} \simeq 10^{10}. \quad (1.1)$$

for a proton near a millisecond pulsar ($\Omega = 10^3 \text{ rad.s}^{-1}$ and $B = 10^5 \text{ T}$), the situation being worst for electron/positron pairs. This ratio corresponds to the number of gyrations made by a particle during the timescale of evolution of the electromagnetic field due to the stellar rotation. It shows that the difference in timescales makes it almost impossible to compute the trajectory of particles in a reasonable amount of time, since billions of time steps are needed on the pulsar period timescale. To tackle this issue, our aim is to propose a new technique based on analytical solutions of the Lorentz force equation in constant and ultra-strong electromagnetic fields meanwhile with an acceptable computational time and most importantly avoiding a necessary scaling, allowing particles to reach high Lorentz factors with realistic fields.

Neutron stars are known to act as unipolar inductors, generating huge electric potential drops between the poles and the equator, of the order

$$\Delta\phi = \Omega B R^2 \approx 10^{16} \text{ V}. \quad (1.2)$$

As a consequence, it expels electrons, maybe protons and ions, filling the magnetosphere with charged particles. Typical Lorentz factor for electrons in this static field are therefore

$$\gamma = \frac{e \Delta\phi}{m_e c^2} \approx 10^{10}. \quad (1.3)$$

If the particle injection rate is high enough, this plasma will screen the electric field, drastically mitigating the potential drop $\Delta\phi$ and the acceleration efficiency. Resistive (Li *et al.* 2012) and PIC simulations (Cerutti *et al.* 2015) showed that indeed only a small fraction of the full potential is available. However, for low particle injection rates, the plasma is unable to screen the electric field and the full potential drop develops. The magnetosphere is then almost empty and known as an electrosphere (Krause-Polstorff & Michel 1985; Pétri *et al.* 2002). Such electrospheres are the subject of the present paper. They represent inactive pulsars able to accelerate particles to ultra-relativistic speeds. We aim at accurately quantifying the final Lorentz factor reached by the outflowing plasma in this large amplitude low frequency electromagnetic wave. Similar studies have been performed by Michel & Li (1999) staying however on a more analytical side.

The outline of the paper is as follows. First in section 2 we briefly remind the principle of the algorithm. Next in section 3 we show some results obtained in fields where an analytical solution is known before discussing the convergence to the exact solution in section 4. Results of the simulations near pulsars are presented in section 5. Some conclusions are drawn in section 6.

2. Outline of the numerical algorithm

In this section we summarize the scheme of our algorithm. A more complete and careful description can be found in Pétri (2020c) with a more comprehensive introduction pointing to appropriate references. The code is based on successive exact analytical solutions for the trajectory of a relativistic particle in a constant but otherwise arbitrary

electromagnetic field (\mathbf{E}, \mathbf{B}) . Switching to a frame where \mathbf{E} and \mathbf{B} are parallel and aligned with the \mathbf{e}_z axis, integration of the Lorentz force in a Cartesian coordinate system $(\mathbf{e}_x, \mathbf{e}_y, \mathbf{e}_z)$ leads to the 4-velocity given by

$$u^0 = \gamma_0 c [\cosh(\omega_E \tau) + \beta_0^z \sinh(\omega_E \tau)] \quad (2.1a)$$

$$u^1 = \gamma_0 c [\beta_0^x \cos(\omega_B \tau) + \beta_0^y \sin(\omega_B \tau)] \quad (2.1b)$$

$$u^2 = \gamma_0 c [-\beta_0^x \sin(\omega_B \tau) + \beta_0^y \cos(\omega_B \tau)] \quad (2.1c)$$

$$u^3 = \gamma_0 c [\sinh(\omega_E \tau) + \beta_0^z \cosh(\omega_E \tau)] \quad (2.1d)$$

and to the 4-position

$$c(t - t_0) = \frac{\gamma_0 c}{\omega_E} [\sinh(\omega_E \tau) + \beta_0^z \cosh(\omega_E \tau) - \beta_0^z] \quad (2.2a)$$

$$x - x_0 = \frac{\gamma_0 c}{\omega_B} [\beta_0^x \sin(\omega_B \tau) - \beta_0^y \cos(\omega_B \tau) + \beta_0^y] \quad (2.2b)$$

$$y - y_0 = \frac{\gamma_0 c}{\omega_B} [\beta_0^x \cos(\omega_B \tau) - \beta_0^x + \beta_0^y \sin(\omega_B \tau)] \quad (2.2c)$$

$$z - z_0 = \frac{\gamma_0 c}{\omega_E} [\cosh(\omega_E \tau) - 1 + \beta_0^z \sinh(\omega_E \tau)]. \quad (2.2d)$$

γ_0 is the initial Lorentz factor, β_0 the initial velocity normalized to the speed of light c , $\omega_E = qE/mc$ and $\omega_B = qB/m$. Integration is performed according to the particle proper time τ . The initial 4-position is (ct_0, x_0, y_0, z_0) .

Note that our treatment proposed above works also for orthogonal fields but not for light-like fields for which both electromagnetic invariants vanish, $I_1 = \mathbf{E} \cdot \mathbf{B} = 0$ and $I_2 = E^2 - c^2 B^2 = 0$. For non light-like fields, we can use the same algorithm, there always exist a frame where either the magnetic field or the electric field vanishes, obtained by a Lorentz boost. For instance the vanishing magnetic field case $\mathbf{B} = \mathbf{0}$ is obtained by taking the limiting $\lim_{\omega_B \rightarrow 0}$ of the above expression thus leading to the 4-velocity

$$u^0 = \gamma_0 c [\cosh(\omega_E \tau) + \beta_0^z \sinh(\omega_E \tau)] \quad (2.3a)$$

$$u^1 = \gamma_0 c \beta_0^x \quad (2.3b)$$

$$u^2 = \gamma_0 c \beta_0^y \quad (2.3c)$$

$$u^3 = \gamma_0 c [\sinh(\omega_E \tau) + \beta_0^z \cosh(\omega_E \tau)] \quad (2.3d)$$

and to the 4-position:

$$c(t - t_0) = \frac{\gamma_0 c}{\omega_E} [\sinh(\omega_E \tau) + \beta_0^z \cosh(\omega_E \tau) - \beta_0^z] \quad (2.4a)$$

$$x - x_0 = \gamma_0 c \beta_0^x \tau \quad (2.4b)$$

$$y - y_0 = \gamma_0 c \beta_0^y \tau \quad (2.4c)$$

$$z - z_0 = \frac{\gamma_0 c}{\omega_E} [\cosh(\omega_E \tau) - 1 + \beta_0^z \sinh(\omega_E \tau)]. \quad (2.4d)$$

In the same way, the vanishing electric field $\mathbf{E} = \mathbf{0}$ is treated with the limit $\lim_{\omega_E \rightarrow 0}$, leading to the 4-velocity

$$u^0 = \gamma_0 c \quad (2.5a)$$

$$u^1 = \gamma_0 c [\beta_0^x \cos(\omega_B \tau) + \beta_0^y \sin(\omega_B \tau)] \quad (2.5b)$$

$$u^2 = \gamma_0 c [-\beta_0^x \sin(\omega_B \tau) + \beta_0^y \cos(\omega_B \tau)] \quad (2.5c)$$

$$u^3 = \gamma_0 c \beta_0^z \quad (2.5d)$$

and to the 4-position

$$c(t - t_0) = \gamma_0 c \tau \quad (2.6a)$$

$$x - x_0 = \frac{\gamma_0 c}{\omega_B} [\beta_0^x \sin(\omega_B \tau) - \beta_0^y \cos(\omega_B \tau) + \beta_0^y] \quad (2.6b)$$

$$y - y_0 = \frac{\gamma_0 c}{\omega_B} [\beta_0^x \cos(\omega_B \tau) - \beta_0^x + \beta_0^y \sin(\omega_B \tau)] \quad (2.6c)$$

$$z - z_0 = \gamma_0 c \beta_0^z \tau. \quad (2.6d)$$

A full derivation of the equations in all field configurations is exposed in Gourgoulhon (2010). In order to decide whether the field is null-like or not, we compare both invariant with the field strength, applying a threshold $\epsilon \ll 1$ such that if $|\mathbf{E} \cdot \mathbf{B}| < \epsilon \|\mathbf{E}\| \|\mathbf{B}\|$ and $|E^2 - c^2 B^2| < \epsilon (E^2 + c^2 B^2)$ the field is said to be light like or null. As long as ϵ is chosen small enough about 10^{-8} or 10^{-12} , the results are insensitive to the precise value of the threshold prescription. Moreover, in most physical applications, the light-like field is rarely met over a large volume in space-time. It happens to be true sometimes at some points but becoming very quickly again non light-like. Especially for our forthcoming applications to PIC code, such condition is highly unlikely. In some of our tests, we impose the external electromagnetic field for instance for a plane wave. In such a case the field is and remains light-like without the plasma feedback, but this situation is highly idealized.

The above mentioned algorithm clearly makes the assumption that the electric and the magnetic fields are constant during a time step $\Delta\tau$ and evaluated at the particle 4-position (t^n, x_i) . The algorithm switches between two reference frames, the first one identified as the observer frame (R) and the second producing an electric field aligned with the magnetic field (R'). Note that a vanishing electric or magnetic field is only a special case included in the former.

At first, in the reference frame (R) of the distant observer, the 4-position \mathbf{X} and 4-velocity \mathbf{U} of the particle is known as well as the electric field \mathbf{E} and the magnetic field \mathbf{B} at the particle's position. We then search for a reference frame (R') in which \mathbf{E}' and \mathbf{B}' are parallel (or, if $\mathbf{E} \cdot \mathbf{B} = 0$, where \mathbf{B}' or \mathbf{E}' vanishes depending on the relative strength of both fields). The speed of frame (R') with respect to frame (R) is noted \mathbf{V} . We align the z-axis of (R) with \mathbf{V} via rotation through the Euler angles, performing a rotation with help on the matrix \mathbf{M}_1 . A Lorentz boost $\Lambda(\mathbf{V})$ switches to the reference frame (R'). In this latter frame the particle's 4-position is \mathbf{X}' and its 4-velocity \mathbf{U}' . We then rotate the axes to align the new z'-axis with \mathbf{E} and \mathbf{B} with the rotation matrix \mathbf{M}_2 . We next update \mathbf{X}' and \mathbf{U}' to the new timestep $(\tau + \Delta\tau)$ thanks to the equations (2.1) and (2.2) describing the trajectory of a particle where the electric and magnetic fields are parallel to the z-axis and assumed to be constant during $\Delta\tau$, with τ the proper time of the particle, u^i the i^{th} component of the four-velocity, β the normalised speed of the particle. Quantities with subscript 0 are initial conditions, and superscripts x, y or z denote a projection on the x, y or z-axis respectively. Once \mathbf{X}' and \mathbf{U}' computed, the frames axes are set back to their initial positions with inverse rotations given by the matrix \mathbf{M}_2^{-1} , the inverse of the \mathbf{M}_2 rotation matrix. We boost back to the reference frame (R) with the inverse Lorentz transformation $\Lambda(-\mathbf{V})$, since in (R') the speed of (R) is $-\mathbf{V}$. And again, we align the axes of (R) with their initial positions thanks to the rotation matrix \mathbf{M}_1^{-1} finding the particle's new 4-position \mathbf{X} and 4-velocity \mathbf{U} .

The special case of the light like field, $\mathbf{E} \cdot \mathbf{B} = 0$ and $E^2 = c^2 B^2$, must be treated separately because there exist no frame where \mathbf{E} and \mathbf{B} are parallel. In the code, to consider that the field is light-like we introduce $\epsilon \ll 1$ and we verify $|E^2 - c^2 B^2| <$

$\epsilon|E^2 + c^2B^2|$ and $|\mathbf{E} \cdot \mathbf{B}| < \epsilon|\mathbf{E}||\mathbf{B}|$ (verification that the cosine of the angle between \mathbf{E} and \mathbf{B} is close to 0). Exact solutions can be found in Pétri (2020c) but they are reminded here for $\omega_B = \omega_E$. In Pétri (2020c) we allow for a more general configuration with $\omega_B = \pm\omega_E$ taking into account possible left or right handed coordinate axes. With \mathbf{B} along \mathbf{e}_z and \mathbf{E} along \mathbf{e}_y , the 4-velocity can directly be obtained by

$$u^0 = \gamma_0 c \left[1 + (1 - \beta_0^x) \frac{(\omega_B \tau)^2}{2} + \beta_0^y \omega_B \tau \right] \quad (2.7a)$$

$$u^1 = \gamma_0 c \left[\beta_0^x + (1 - \beta_0^x) \frac{(\omega_B \tau)^2}{2} + \beta_0^y \omega_B \tau \right] \quad (2.7b)$$

$$u^2 = \gamma_0 c \left[\beta_0^y + (1 - \beta_0^x) \omega_B \tau \right] \quad (2.7c)$$

$$u^3 = \gamma_0 c \beta_0^z \quad (2.7d)$$

as well as the 4-position

$$c(t - t_0) = \gamma_0 c \left[\tau + (1 - \beta_0^x) \frac{\omega_B^2 \tau^3}{6} + \beta_0^y \frac{\omega_B \tau^2}{2} \right] \quad (2.8a)$$

$$x - x_0 = \gamma_0 c \left[\beta_0^x \tau + (1 - \beta_0^x) \frac{\omega_B^2 \tau^3}{6} + \beta_0^y \frac{\omega_B \tau^2}{2} \right] \quad (2.8b)$$

$$y - y_0 = \gamma_0 c \left[\beta_0^y \tau + (1 - \beta_0^x) \frac{\omega_B \tau^2}{2} \right] \quad (2.8c)$$

$$z - z_0 = \gamma_0 c \beta_0^z \tau. \quad (2.8d)$$

Here the algorithm is simpler: the 4-position \mathbf{X} , the 4-velocity \mathbf{U} of the particle are known, as well as \mathbf{E} and \mathbf{B} felt by the particle. We then perform a rotation of matrix \mathbf{M} to align \mathbf{E} with \mathbf{e}_z and \mathbf{B} with \mathbf{e}_y . Next we directly update the particles 4-position \mathbf{X} and 4-velocity \mathbf{U} to the next timestep ($\tau + \Delta\tau$) and we then rotate back to the initial set of axes with \mathbf{M}^{-1} .

It is important to note that this peculiar case is very uncommon in the simulations mentioned in 5. Indeed, when choosing $\epsilon = 10^{-15}$, the algorithm never used this peculiar case. In fact, the light-like case is only found in very precise positions or far from the neutron star, at distances the particles did not reached by the end of the simulations and this part of the algorithm was added so as to be able to work in any field, especially plane waves.

Technically, for the computation of the new velocity and position, a convergence criterion is applied on the electromagnetic field to make sure that the assumption \mathbf{E} and \mathbf{B} remaining almost constant is verified to a prescribed accuracy. To do so, we use a loop on the \mathbf{E} and \mathbf{B} fields: at first we move the particle at the 4-position (ct, x, y, z) by taking $\mathbf{E}_0 = \mathbf{E}(t, x, y, z)$ and $\mathbf{B}_0 = \mathbf{B}(t, x, y, z)$, so the particle's 4-position becomes $(c(t+dt_0), x+dx_0, y+dy_0, z+dz_0)$. Then, we make the particle start again from (ct, x, y, z) but we take the averaged fields: $\mathbf{E}_1 = \mathbf{E}(t+dt_0/2, x+dx_0/2, y+dy_0/2, z+dz_0/2)$ and $\mathbf{B}_1 = \mathbf{B}(t+dt_0/2, x+dx_0/2, y+dy_0/2, z+dz_0/2)$ for the incrementation of the time, updating the 4-position: $(c(t+dt_1), x+dx_1, y+dy_1, z+dz_1)$. Then again, the particle starts from (ct, x, y, z) and we increment the time step with the fields being $\mathbf{E}_2 = \mathbf{E}(t+dt_1/2, x+dx_1/2, y+dy_1/2, z+dz_1/2)$ and $\mathbf{B}_2 = \mathbf{B}(t+dt_1/2, x+dx_1/2, y+dy_1/2, z+dz_1/2)$. Generally, for $k \neq 0$ incrementing the time step with the field \mathbf{E}_k and \mathbf{B}_k returns the 4-position $(c(t+dt_k), x+dx_k, y+dy_k, z+dz_k)$, and the fields are defined as $\mathbf{E}_{k+1} = \mathbf{E}(t+dt_k/2, x+dx_k/2, y+dy_k/2, z+dz_k/2)$ and $\mathbf{B}_{k+1} = \mathbf{B}(t+dt_k/2, x+dx_k/2, y+dy_k/2, z+dz_k/2)$. We keep the loop going while $\mathbf{B}_k \neq \mathbf{B}_{k-1}$

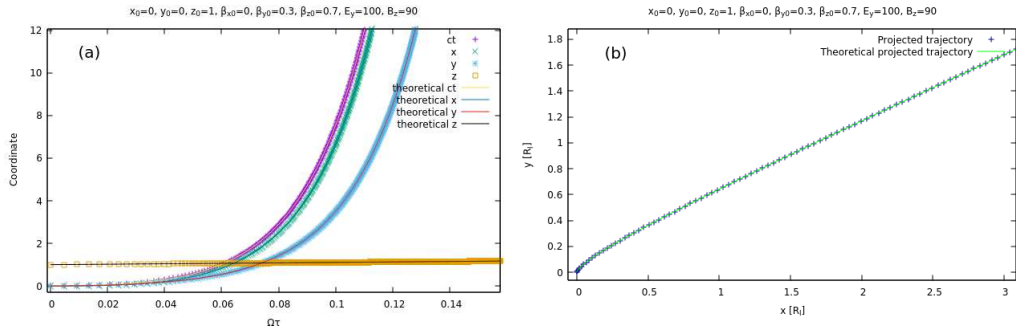


Figure 1: Evolution of a particle in a dominant electric field, $x_0 = 0, y_0 = 0, z_0 = 1, \beta_{x_0}^x = 0, \beta_{y_0}^y = 0.3, \beta_{z_0}^z = 0.7, \frac{qE_y}{cm} = 100, \frac{qB_z}{m} = 90$. Theoretical and simulated 4-position as function of the proper time τ (a). Projection of the trajectory of the particle in the x-y plane (b).

and $\mathbf{E}_k \neq \mathbf{E}_{k-1}$, which numerically translates to $|E_k^j - E_{k-1}^j| > \epsilon(|E_k^j| + |E_{k-1}^j|)$ and $|B_k^j - B_{k-1}^j| > \epsilon(|B_k^j| + |B_{k-1}^j|)$, with $\epsilon \ll 1$ (we chose $\epsilon = 10^{-4}$), and $j = \{x, y, z\}$.

As a check of the implementation of our new algorithm, simulations were performed either in a constant and uniform field, or in a plane electromagnetic wave. Once passing the tests, we applied our code to realistic astrophysical cases of rotating neutron stars using the Deutsch (1955) field solution, neglecting so far radiation reaction that will be included in a next step.

3. Test cases

We carried some simulations to test the code in cases where the trajectory of the particle is known analytically. Simple checks with only an electric or magnetic field or both were made, allowing for orthogonal or parallel geometries.

When the \mathbf{E} and \mathbf{B} fields are parallel, in addition to the gyration around the magnetic field lines, the particle is accelerated along the electric field, so that particles describe an helix getting elongated as time goes, if not at first slowing down if its initial velocity is in a direction opposite to its acceleration.

If \mathbf{E} and \mathbf{B} are orthogonal (as in figure 1, figure 2 and figure 3, where \mathbf{E} is along the y-axis and \mathbf{B} along the z-axis), three cases are possible:

- \mathbf{E} dominant shown in figure 1 where the particle is accelerated along the \mathbf{E} field but also drifts along $\mathbf{E} \times \mathbf{B}/E^2$.
- \mathbf{B} dominant, as in figure 2 where the particles moves in a cycloidal motion with the component of its speed along \mathbf{E} switching between aligned and anti aligned, and the other component being again a drift along $\mathbf{E} \times \mathbf{B}/B^2$.
- in the special case of the light-like field ($\mathbf{E} \cdot \mathbf{B} = 0$ and $E^2 = c^2 B^2$), in figure 3, where the trajectory of the particle is not periodic, in a similar fashion as the case \mathbf{E} dominant with an increasing speed along \mathbf{B} and again a drift along $\mathbf{E} \times \mathbf{B}$.

In addition to the tests in constant uniform fields, simulations were made with linearly and circularly polarised plane electromagnetic waves, for which exact solutions are known (Uzan & Deruelle 2014).

Consider a linearly polarized plane wave propagating along the \mathbf{e}_x direction such that the 4-vector potential is $A^\alpha = (0, 0, \frac{E}{\omega} \cos \xi, 0)$. The phase is $\xi = \omega t - kx$. The

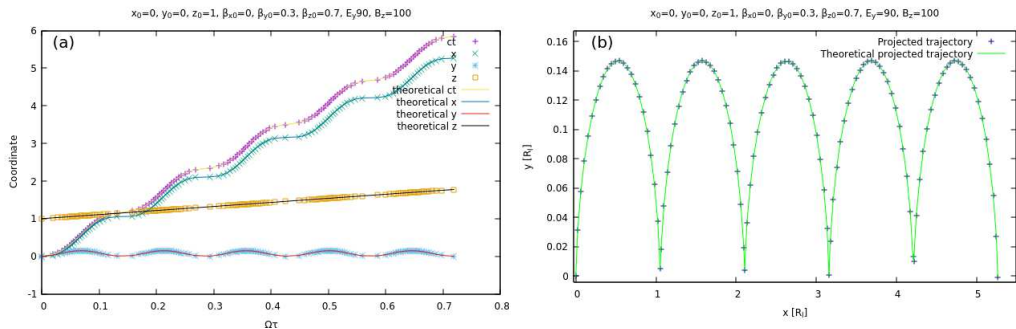


Figure 2: Evolution of a particle in a dominant magnetic field, $x_0 = 0$, $y_0 = 0$, $z_0 = 1$, $\beta_0^x = 0$, $\beta_0^y = 0.3$, $\beta_0^z = 0.7$, $\frac{qE_y}{mc} = 90$, $\frac{qB_z}{m} = 100$. Theoretical and simulated 4-position as function of the proper time τ (a). Projection of the trajectory of the particle in the x-y plane (b).

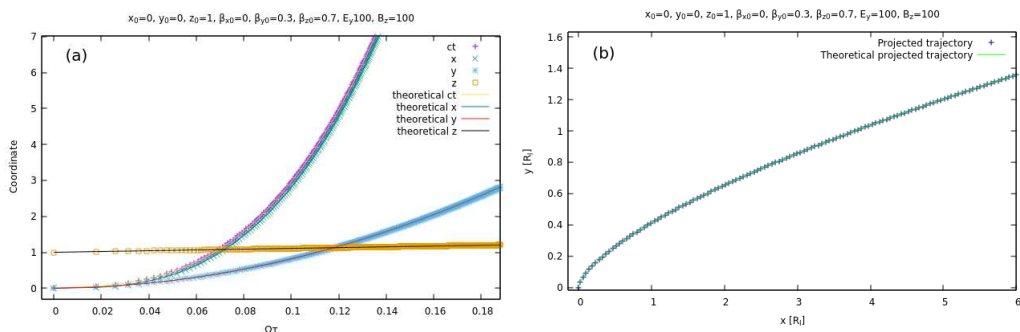


Figure 3: Evolution of a particle in a light-like field, $x_0 = 0$, $y_0 = 0$, $z_0 = 1$, $\beta_0^x = 0$, $\beta_0^y = 0.3$, $\beta_0^z = 0.7$, $\frac{qE_y}{cm} = 100$, $\frac{qB_z}{m} = 100$. Theoretical and simulated 4-position as function of the proper time τ (a). Projection of the trajectory of the particle in the x-y plane (b).

electromagnetic field is given by

$$\mathbf{E} = E \sin \xi \mathbf{e}_y \quad (3.1a)$$

$$\mathbf{B} = \frac{E}{c} \sin \xi \mathbf{e}_z. \quad (3.1b)$$

Initially the particle is at rest with a 4-velocity $u_0^\alpha = (c, \mathbf{0})$. Introducing the strength parameter of the wave by the ratio

$$a = \frac{qE}{mc\omega} \quad (3.2)$$

the 4-velocity has components

$$u^x = \frac{a^2}{2} c (\cos \xi - 1)^2 \quad (3.3a)$$

$$u^y = -a c (\cos \xi - 1) \quad (3.3b)$$

$$u^0 = c + u^x. \quad (3.3c)$$

The Lorentz factor is deduced from $\gamma c = u^0$.

Consider now a circularly polarized plane wave propagating in the \mathbf{e}_x direction such that the vector potential has components $A^\alpha = (0, 0, \frac{E}{\omega} \cos \xi, \frac{E}{\omega} \sin \xi)$ and the phase $\xi = \omega t - kx$. The electromagnetic field is then given by

$$\mathbf{E} = E (\sin \xi \mathbf{e}_y - \cos \xi \mathbf{e}_z) \quad (3.4a)$$

$$\mathbf{B} = \frac{E}{c} (\sin \xi \mathbf{e}_z + \cos \xi \mathbf{e}_y). \quad (3.4b)$$

Initially the particle is at rest with 4-velocity $u_0^\alpha = (c, \mathbf{0})$. The time evolution of the components of this 4-velocity will be

$$u^x = a^2 c (1 - \cos \xi) = a u^y \quad (3.5a)$$

$$u^y = a c (1 - \cos \xi) \quad (3.5b)$$

$$u^z = -a c \sin \xi \quad (3.5c)$$

$$u^0 = c + u^x. \quad (3.5d)$$

Simulations of linearly and circularly polarized plane waves were carried out as shown in figure 4 and figure 5. In these waves, the particle undergoes a series of acceleration and braking.

The particle's Lorentz factor reaches a maximum value of

$$\gamma = 1 + 2a^2 \quad (3.6)$$

This shows that the code works well in ultra-strong fields with little to no error.

In addition, the cases of elliptically polarized waves can be treated in the code. The equation of the fields of such waves is given by

$$\mathbf{E} = E (\sin \xi \mathbf{e}_y - \alpha \cos \xi \mathbf{e}_z) \quad (3.7a)$$

$$\mathbf{B} = \frac{E}{c} (\sin \xi \mathbf{e}_z + \alpha \cos \xi \mathbf{e}_y). \quad (3.7b)$$

With $0 \leq \alpha \leq 1$. The case $\alpha = 1$ gives the circular wave whereas the case $\alpha = 0$ returns the linearly polarized wave. For any kind of polarization, the maximum Lorentz factor of the particle is still $\gamma = 1 + 2a^2$ however the evolution of the particle's Lorentz factor is the following

$$\gamma = 1 + a^2 (1 - \cos \xi) - \frac{a^2}{2} (1 - \alpha^2) \sin^2 \xi \quad (3.8)$$

which is equation (157) of Michel & Li (1999) except for a typo in the sign of the last term. More details about plane waves and how to find these equations can be found in Michel & Li (1999).

In the case of plane electromagnetic waves other algorithms have trouble at strength parameters above $a = 25$ Arefiev *et al.* (2015) whereas our scheme easily exceeds this value of a with short computational times.

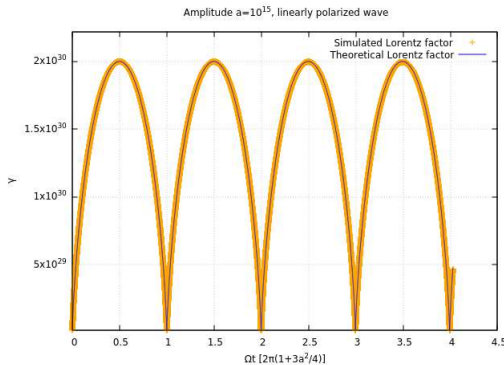


Figure 4: Lorentz factor of a particle in a linearly polarised plane electromagnetic wave of strength parameter $a = 10^{15}$.

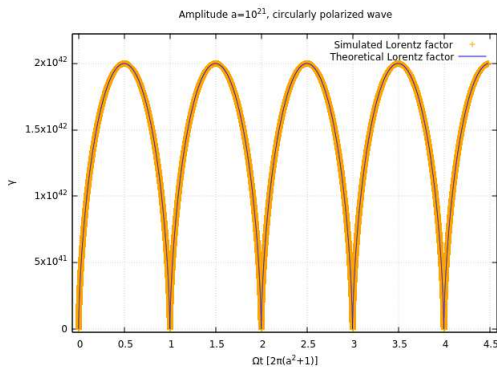


Figure 5: Lorentz factor of a particle in a circularly polarised plane electromagnetic wave of strength parameter $a = 10^{21}$.

4. Convergence and error of the algorithm

We study the convergence of our algorithm in simple test cases where analytical solutions are known. For instance, let us track a particle of charge q and mass m subject to an acceleration in an electric field \mathbf{E} assumed to grow linearly in proper time τ such that

$$\mathbf{E}(\tau) = E(\tau)\mathbf{e}_z \quad (4.1)$$

with

$$\frac{q}{mc}E(\tau) = \alpha\tau. \quad (4.2)$$

We choose this form of field since a constant field will give no error, for the code is based on analytical solutions in constant fields. At $\tau = 0$, the particle is at $x^\mu = (0 \ 0 \ 0 \ 0)$ and its 4-velocity is $u^\mu = (c \ 0 \ 0 \ 0)$. In this configuration, the Faraday tensor is

$$F^{\mu\nu} = \begin{pmatrix} 0 & 0 & 0 & -E(\tau)/c \\ 0 & 0 & 0 & 0 \\ 0 & 0 & 0 & 0 \\ E(\tau)/c & 0 & 0 & 0 \end{pmatrix}. \quad (4.3)$$

Starting from the equation of motion:

$$\frac{du^\mu}{d\tau} = \frac{q}{m} F^{\mu\nu} u_\nu \quad (4.4)$$

When looking only at u^t and u^z we find

$$\frac{du^t}{d\tau} = -\frac{qE(\tau)}{mc} u_z = -\alpha\tau u_z = \alpha\tau u^z \quad (4.5a)$$

$$\frac{du^z}{d\tau} = \frac{qE(\tau)}{mc} u_t = \alpha\tau u_t = \alpha\tau u^t \quad (4.5b)$$

We then define

$$\Delta = u^t - u^z \quad (4.6a)$$

$$\Sigma = u^t + u^z \quad (4.6b)$$

So we can obtain with (4.5a)-(4.5b) and (4.5a)+(4.5b)

$$\frac{d\Delta}{d\tau} = -\alpha\tau\Delta \quad (4.7a)$$

$$\frac{d\Sigma}{d\tau} = \alpha\tau\Sigma \quad (4.7b)$$

Which solves into

$$\Delta(\tau) = \delta e^{-\alpha\tau^2/2} \quad (4.8a)$$

$$\Sigma(\tau) = \sigma e^{\alpha\tau^2/2} \quad (4.8b)$$

At $\tau = 0$, we find:

$$\delta = \sigma = \gamma_0 \quad (4.9)$$

Noticing that

$$u^t = \frac{\Sigma + \Delta}{2} = \gamma_0 \frac{e^{\alpha\tau^2/2} + e^{-\alpha\tau^2/2}}{2} \quad (4.10a)$$

$$u^z = \frac{\Sigma - \Delta}{2} = \gamma_0 \frac{e^{\alpha\tau^2/2} - e^{-\alpha\tau^2/2}}{2} \quad (4.10b)$$

So the expression of the Lorentz factor and the four velocity along z are:

$$u^t = \gamma_0 c \cosh(\alpha\tau^2/2) \quad (4.11a)$$

$$u^z = \gamma_0 c \sinh(\alpha\tau^2/2) \quad (4.11b)$$

After another integration, we get the position of the particle:

$$ct = \gamma_0 c \sqrt{\frac{\pi}{8\alpha}} [\operatorname{erf}(\tau\sqrt{\alpha/2}) + \operatorname{erfi}(\tau\sqrt{\alpha/2})] \quad (4.12a)$$

$$z = \gamma_0 c \sqrt{\frac{\pi}{8\alpha}} [\operatorname{erfi}(\tau\sqrt{\alpha/2}) - \operatorname{erf}(\tau\sqrt{\alpha/2})] \quad (4.12b)$$

Where erf and erfi are defined (with i the imaginary unit):

$$\operatorname{erf}(\tau) = \frac{2}{\sqrt{\pi}} \int_0^\tau \exp(-t^2) dt \quad (4.13a)$$

$$\operatorname{erfi}(\tau) = \frac{\operatorname{erf}(i\tau)}{i} \quad (4.13b)$$

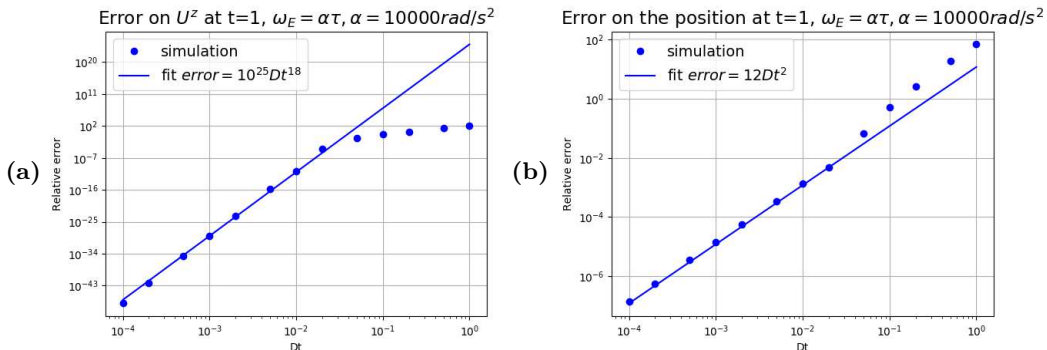


Figure 6: Relative error on the speed and on the position of the particle in an electric field aligned with \mathbf{e}_z where $\omega_E = \alpha\tau$, $\alpha = 10^4$.

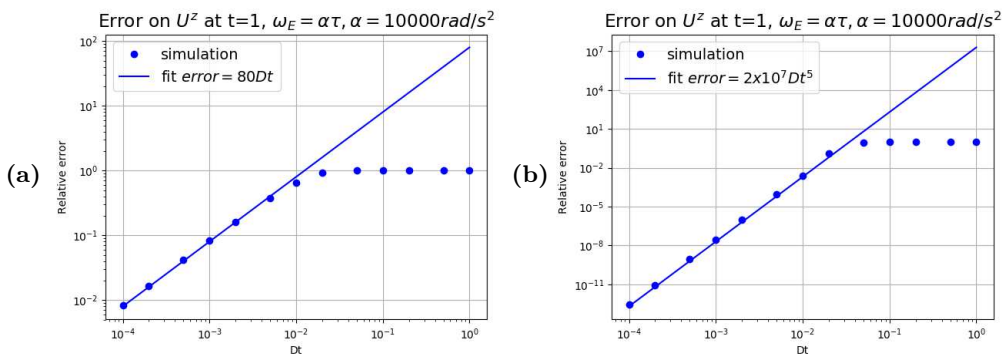


Figure 7: Relative error on the speed of the particle in an electric field aligned with \mathbf{e}_z where $\omega_E = \alpha\tau$, $\alpha = 10^4$. (a) No convergence loop on the field. (b) At most three run in the convergence loop.

When comparing (4.11b) and (4.12b) to the outcome of the simulations, we can get the error $\delta\alpha$ thanks to the following formula:

$$\delta\alpha = \frac{|\alpha_{measured} - \alpha_{theoretical}|}{|\alpha_{theoretical}|}, \quad (4.14)$$

when α is taken to be u^z or z we obtain the the plots of figure 6, highlighting a fast decrease on the error on the 4-velocity however the error on the 4-position shows that the scheme of the simulation is of order 2.

A more in-depth analysis showed that the number of run through the field convergence loop discussed in 2 has an influence on the order of the algorithm, explaining why such a high order is found on figure 6. Simulations where no convergence is applied or where at most three runs through the convergence loop are made are respectively of order 1 or 5, as shown by figure 7.

Other studies of the rate of convergence to the analytical solutions can be found in Pétri (2020c) for a linearly and a circularly polarized wave. There it is shown that the error is second order in time.

5. Rotating neutron star fields

5.1. Vacuum rotating electromagnetic field solution

Eventually we implemented the Deutsch field in our code in order to mimic a rotating magnet in vacuum. The exact solution for the rotating dipole in vacuum is given by Deutsch (1955). The corresponding electromagnetic field, written in a complex form, reads

$$B_r(\mathbf{r}, t) = 2B \left[\frac{R^3}{r^3} \cos \chi \cos \vartheta + \frac{R}{r} \frac{h_1^{(1)}(kr)}{h_1^{(1)}(kR)} \sin \chi \sin \vartheta e^{i\psi} \right] \quad (5.1a)$$

$$B_\vartheta(\mathbf{r}, t) = B \left[\frac{R^3}{r^3} \cos \chi \sin \vartheta + \right. \quad (5.1b)$$

$$\left. \left(\frac{R}{r} \frac{d}{dr} \left(r h_1^{(1)}(kr) \right) + \frac{R^2}{r_L^2} \frac{h_2^{(1)}(kr)}{\frac{d}{dr} \left(r h_2^{(1)}(kr) \right) |_R} \right) \sin \chi \cos \vartheta e^{i\psi} \right] \quad (5.1c)$$

$$B_\varphi(\mathbf{r}, t) = B \left[\frac{R}{r} \frac{d}{dr} \left(r h_1^{(1)}(kr) \right) + \frac{R^2}{r_L^2} \frac{h_2^{(1)}(kr)}{\frac{d}{dr} \left(r h_2^{(1)}(kr) \right) |_R} \cos 2\vartheta \right] i \sin \chi e^{i\psi} \quad (5.1d)$$

$$E_r(\mathbf{r}, t) = \Omega B R \left[\left(\frac{2}{3} - \frac{R^2}{r^2} (3 \cos^2 \vartheta - 1) \right) \frac{R^2}{r^2} \cos \chi \right. \\ \left. + 3 \sin \chi \sin 2\vartheta e^{i\psi} \frac{R}{r} \frac{h_2^{(1)}(kr)}{\frac{d}{dr} \left(r h_2^{(1)}(kr) \right) |_R} \right] \quad (5.1e)$$

$$E_\vartheta(\mathbf{r}, t) = \Omega B R \left[-\frac{R^4}{r^4} \sin 2\vartheta \cos \chi + \sin \chi e^{i\psi} \left(\frac{R}{r} \frac{d}{dr} \left(r h_2^{(1)}(kr) \right) \cos 2\vartheta - \frac{h_1^{(1)}(kr)}{h_1^{(1)}(kR)} \right) \right] \quad (5.1f)$$

$$E_\varphi(\mathbf{r}, t) = \Omega B R \left[\frac{R}{r} \frac{d}{dr} \left(r h_2^{(1)}(kr) \right) - \frac{h_1^{(1)}(kr)}{h_1^{(1)}(kR)} \right] i \sin \chi \cos \vartheta e^{i\psi} \quad (5.1g)$$

where $h_\ell^{(1)}$ are the spherical Hankel functions for outgoing waves (Arfken & Weber 2005), $kr_L = 1$ and the phase is $\psi = -\Omega t$. An example of magnetic field lines for a perpendicular rotator is shown in figure 8.

Our aim for these simulations was to investigate the behaviour of particles close to the neutron star, especially to find the final Lorentz factor the particles were able to reach as well as the influence of their initial position on their final position and energy.

As expected, the particles could either be ejected far from the neutron star reaching an almost ballistic trajectory or crash onto the neutron star surface or be trapped around the pulsar.

In all of our simulations, we work with a millisecond pulsar for which $r_L = 10R = 100$ km so $\Omega = 3000$ rad.s⁻¹ and the period is about $P \approx 2.1$ ms. We choose the magnetic field strength at the equator to be $B = 10^5$ T.

5.2. Settings

The main purpose of our simulations was to investigate the evolution of five types of particles: electrons, protons, antiprotons, fully ionized iron ⁵⁶Fe and fictive particles with

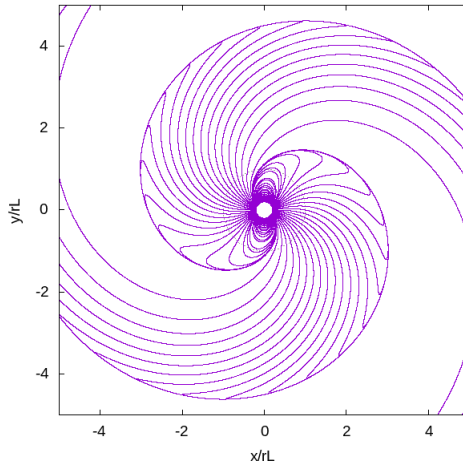


Figure 8: Magnetic field line of an orthogonal rotator with $r_L = 5R$.

the charge of a proton, but 10^6 times its mass (mentioned in 5.3.1). The inclination angle of the neutron stars is taken in the set $\chi = \{0^\circ, 30^\circ, 60^\circ, 90^\circ, 120^\circ, 150^\circ, 180^\circ\}$.

We tried three different initial set ups by imposing the starting positions of the particles

(i) The first set up used 2.048 particles for each obliquity and type of charges, following the same regular pattern. These particles were distributed uniformly in spherical coordinates, radius ($r = (2+k)R$, $k \in \llbracket 0; 7 \rrbracket$), colatitude ($\theta = \frac{l}{9}\pi$, $l \in \llbracket 1; 8 \rrbracket$) and azimuth ($\phi = \frac{m}{16}\pi$, $m \in \llbracket 0; 31 \rrbracket$). (Note that this does not correspond to a uniform distribution in space.)

(ii) The second set up also used 2.048 particles per obliquity. However, they were randomly placed in space. The radius follows a uniform distribution $r \in [2R; 10R]$, the azimuth ϕ also follows a uniform distribution $\phi \in [0; 2\pi]$, however, for the colatitude, we use another variable u , following a uniform probability $u \in [0; 1]$ and then we set the initial colatitude of the particle to be $\theta = \arccos(1 - 2u)$ so as to avoid artificial particles overdensities close to the rotation axis because of the singularity along this axis.

(iii) The third set up only used protons, but with 16.384 particles for each inclination, with the same random distribution as in point (ii).

Unless they crashed onto the neutron star, these test particles were free to evolve for a time $T = 15 \Omega^{-1}$ in normalised units which is $T = 5 \text{ ms} \simeq 2.39$ periods.

5.3. Regularly placed particles

5.3.1. Particle distribution functions and symmetries

The particle distribution functions $f(\gamma) = dN(\gamma)/d\gamma$, where $dN(\gamma)$ is the number of particles with Lorentz factor in the range $[\gamma, \gamma + d\gamma]$, and final positions are shown in figure 9. For particles of the same mass m but opposite charge $\pm q$, the behaviour is symmetric, meaning that if for an inclination χ a proton starts at position (r_i, θ_i, ϕ_i) and ends at position (r_f, θ_f, ϕ_f) , for an inclination such that $\chi' = \pi - \chi$ an antiproton with an initial position $(r'_i = r_i, \theta'_i = \pi - \theta_i, \phi'_i = \phi_i)$ will end at $(r'_f = r_f, \theta'_f = \pi - \theta_f, \phi'_f = \phi_f)$. Thus we only need to investigate particles of one charge, let it be leptons or their antiparticles, which is expected according to symmetry arguments discussed in Laue & Thielheim (1986). Another symmetry relative to the centre of the neutron star is also noticeable in figure 9, figure 12 and figure 14 and tells us that for an inclination χ , if

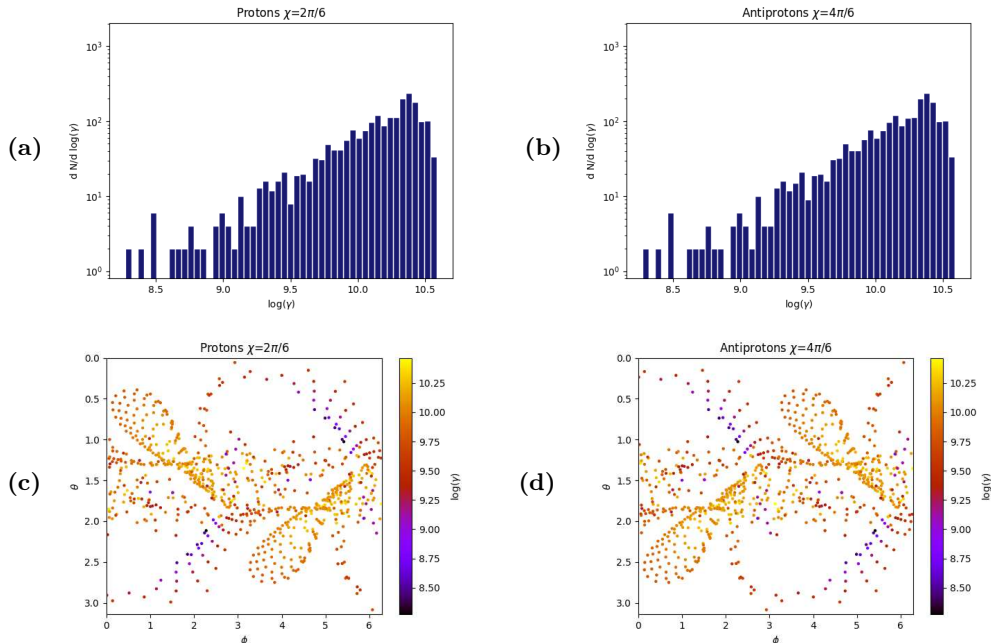


Figure 9: Comparison between protons around a pulsar of inclination $\chi = 60^\circ$, and antiprotons around a pulsar of inclination $\chi = 120^\circ$ to highlight their symmetrical behaviour. (a) Proton Lorentz factor spectra. (b) Antiproton Lorentz factor spectra. (c) Proton ejection map. (d) Antiproton ejection map. The ejection maps are the final latitudes θ and azimuths ϕ of particles that went beyond the light cylinder. These particles have an almost radial trajectory.

a particle is injected in (r_i, θ_i, ϕ_i) and ends at (r_f, θ_f, ϕ_f) , a particle injected in $(r_i, \pi - \theta_i, \pi + \phi_i)$ will end at $(r_f, \pi - \theta_f, \pi + \phi_f)$. Again this was discussed in Laue & Thielheim (1986).

5.3.2. Final Lorentz factors

In the simulations, we explored the dependence of the final Lorentz factor with respect to the particle charge to mass ratio q/m . Results of our computations showed that the iron ^{56}Fe reaches Lorentz factors of $\gamma_{\text{Fe}} \sim 10^{10.5}$, protons and antiprotons up to $\gamma_p \sim 10^{10.7}$ while electrons up to $\gamma_e \sim 10^{14}$. As a check for the scaling we also tried fictive particles of artificially very high mass $m_{\text{Mp}} = 10^6 m_p$ and charge $q_{\text{Mp}} = q_p = +e$ reaching only Lorentz factors up to $\gamma_{\text{Mp}} \sim 10^{4.7}$.

As anticipated particles with high charge to mass ratio are accelerated more efficiently. In fact the different spectra have similar shapes simply shifted along the $\log(\gamma)$ axis. This is visible by comparing for instance figure 10a and figure 10b showing the distribution functions for iron and protons respectively. For these spectra, the difference is $\Delta \log(\gamma) \sim 0.33 \sim \log(2.15)$ meaning that $\gamma_p \sim 2.15 \gamma_{\text{Fe}}$. When comparing figure 10b to figure 10d for protons and massive particles, the shift is $\Delta \log(\gamma) \sim 6$ so $\gamma_p \sim 10^6 \gamma_{\text{Mp}}$.

Just like for protons and iron nuclei, and taking into account the symmetrical behaviour of particles of opposite charge, Lorentz factor distribution functions of protons and electrons show alike features for inclination such as $\chi_e = \pi - \chi_p$ (χ_e is the inclination of

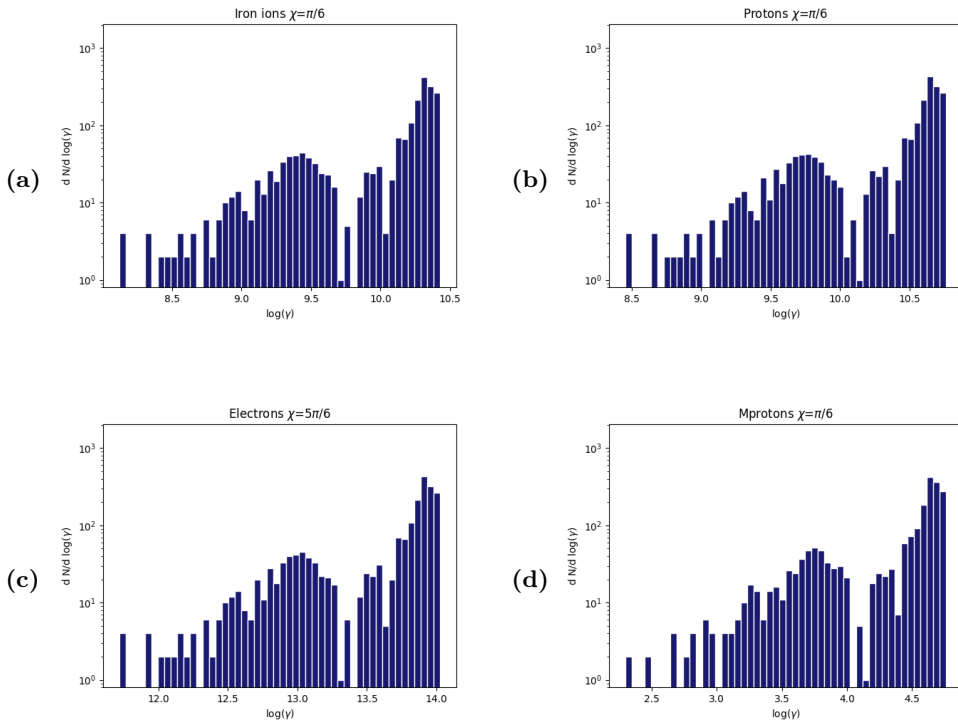


Figure 10: Comparison of different particle distribution functions following the regular placement: (a) ^{56}Fe ions around a pulsar of inclination $\chi = 30^\circ$, (b) Protons around a pulsar of inclination $\chi = 30^\circ$, (c) Electrons around a pulsar of inclination $\chi = 150^\circ$, (d) Fictive particle ($q_{Mp} = q_p$, $m_{Mp} = 10^6 m_p$) around a pulsar of inclination $\chi = 30^\circ$.

the pulsar for the electron and χ_p for the proton) but shifted by an amount $\Delta \log(\gamma) \sim 3.3 \sim \log(1836)$, compare figure 10c with figure 10b.

As an example, in figure 10b with protons, when $\chi = \frac{\pi}{6}$, two lobes are visible in the spectrum: one from $\log(\gamma) = 8.3$ to $\log(\gamma) = 10.1$ and the other from $\log(\gamma) = 10.2$ to $\log(\gamma) = 10.7$. For electrons in figure 10c, with $\chi = \frac{5\pi}{6}$ the lobes also appear but from $\log(\gamma) = 11.6$ to $\log(\gamma) = 13.5$ and from $\log(\gamma) = 13.5$ to $\log(\gamma) = 14$. This difference show that $\gamma_e \sim 1836\gamma_p$ (γ_e is the Lorentz factor of electrons) for $\chi_e = \pi - \chi_p$.

Noticing the following ordering

$$\frac{q_p/m_p}{q_{Fe}/m_{Fe}} = \frac{56}{26} \sim 2.154 \quad , \quad \frac{|q_e/m_e|}{|q_p/m_p|} \sim 1836 \quad , \quad \frac{q_p/m_p}{q_{Mp}/m_{Mp}} = 10^6 \quad (5.2)$$

we conclude that the final Lorentz factor of the test particles is proportional to the strength parameter of these particles, as long as they are relativistic.

In complement, the spectra were analysed depending on whether the particles were ejected, trapped or crashed like in figure 11. For protons, at inclinations $\chi = \{0, \frac{\pi}{6}, \frac{\pi}{3}\}$ the most energetic particles were those falling on the neutron star (at $\chi = 0^\circ$ all particles crashed with $10.3 \leq \log(\gamma) \leq 10.8$). For $\chi = 30^\circ$ falling particles are responsible for the high Lorentz factor lobe of the spectra. At $\chi = 90^\circ$ however, crashing particles had similar energies as the ejected or trapped ones.

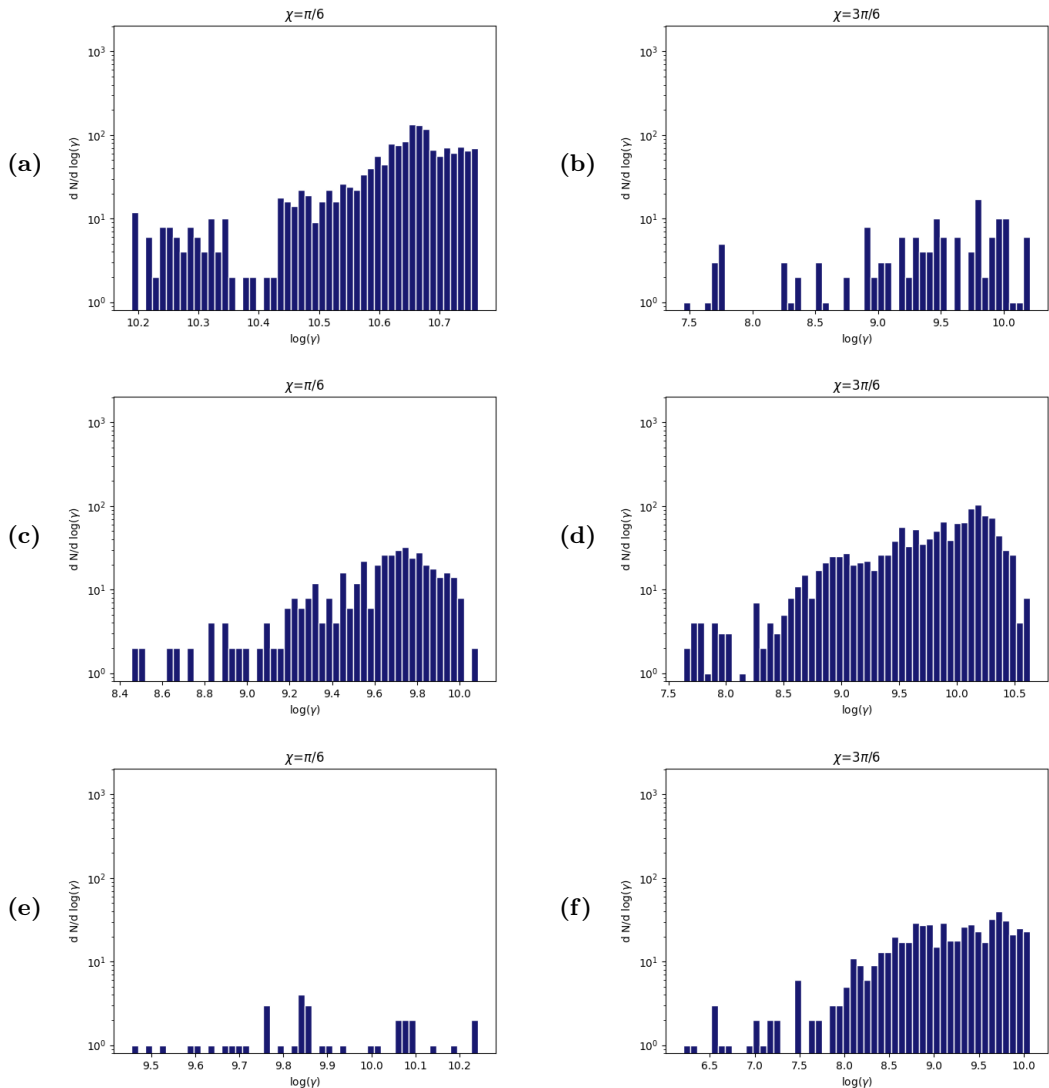


Figure 11: Proton distribution functions depending on their final state. (a) Crashed, $\chi = 30^\circ$, (b) Crashed, $\chi = 90^\circ$, (c) Ejected, $\chi = 30^\circ$, (d) Ejected, $\chi = 90^\circ$, (e) Trapped, $\chi = 30^\circ$, (f) Trapped, $\chi = 90^\circ$, for a regular pattern of particles.

5.3.3. Positions of particles

The same trajectory of antiprotons and electrons despite their mass difference is visible in figure 12. Our guess is that the magnetic field is so strong that particles are forced to follow the same magnetic field lines and only a low charge to mass ratio particle could have a different trajectory since it would be accelerated less efficiently and take more time to reach a speed close to c .

In addition, plotting the Lorentz factor map of the particles depending on their initial position shows that some areas are more prone to particle acceleration and that these regions are not randomly distributed and follow well a central symmetry, see figure 13. These maps highlighted however some issues since a few particles did not follow exactly

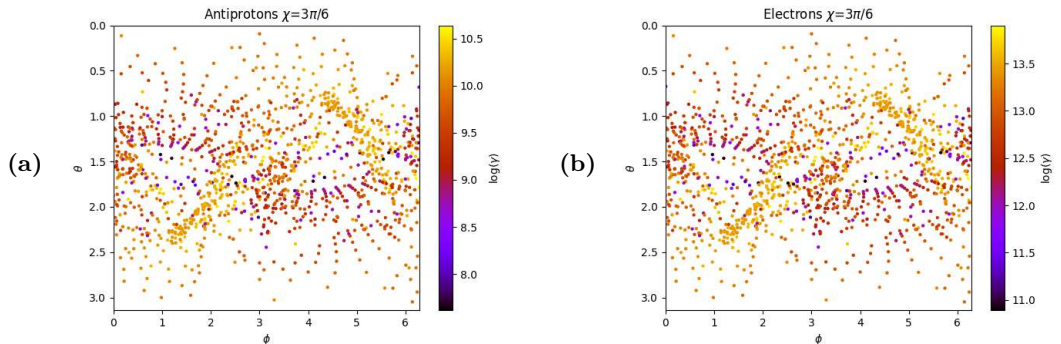


Figure 12: Ejection maps of antiprotons (a) and electrons (b) for $\chi = 90^\circ$. Regular pattern placement.

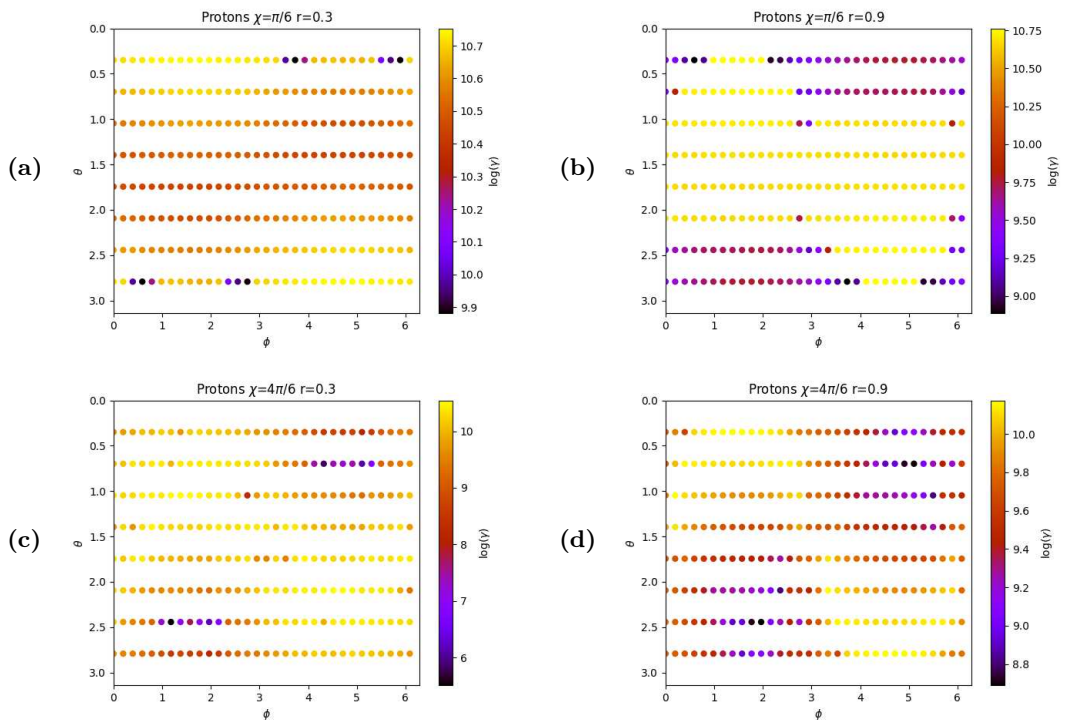


Figure 13: Final Lorentz factor of the protons depending on their initial positions, for several pulsar inclinations and a given radius of injection of the particles: (a) $r_0 = 0.3r_L$, $\chi = 30^\circ$, (b) $r_0 = 0.9r_L$, $\chi = 30^\circ$, (c) $r_0 = 0.3r_L$, $\chi = 120^\circ$, (d) $r_0 = 0.9r_L$, $\chi = 120^\circ$.

the central symmetry, meaning that computationally speaking, some errors tend to appear during the simulations.

Finally, aside when $\chi = 90^\circ$ only particles with a charge of a given sign could fall onto the neutron star. Indeed particles with positive charge crashed for $0^\circ \leq \chi \leq 90^\circ$ and those with negative charge for $90^\circ \leq \chi \leq 180^\circ$. When investigating their final coordinates, and taking into account the delay between the start of the simulation and

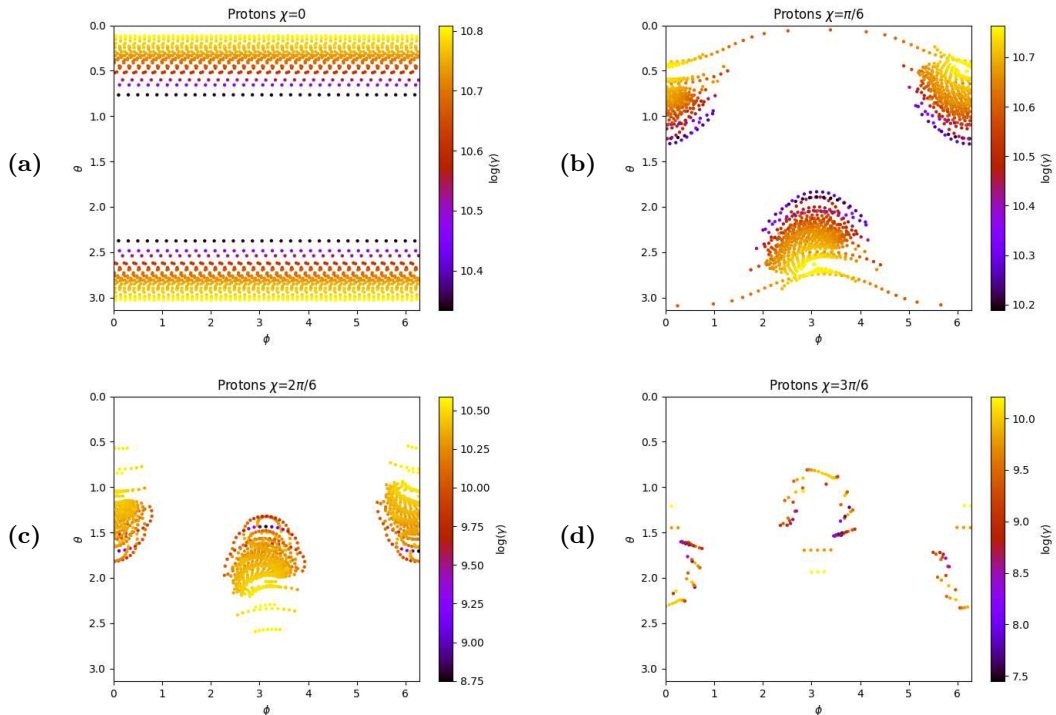


Figure 14: Impact maps of protons on the neutron star surface for $\chi = 0^\circ$ (a), $\chi = 30^\circ$ (b), $\chi = 60^\circ$ (c) and $\chi = 90^\circ$ (d). Regular placement of particles.

the time the particles hit the surface, the impact maps show that the particles form hotspots around the magnetic axis instead of randomly hitting the surface, as figure 14 shows.

5.4. Randomly placed particles

5.4.1. Lorentz factor of the particles

The simulations with randomly placed particles were useful for the spectral analysis in complement to those of 5.3.2. Indeed, figure 15a allows us to get rid of the "gap" in the high energy lobe that is visible otherwise in figure 10b while keeping the two distinct lobes. Otherwise, the overall tendencies of spectra were those discussed in 5.3.2. A deeper analysis with more particle yields the results shown in figure 16 with even smoother spectra and filling more the low energy end of the spectra.

In a similar way, comparing figure 17 to figure 11 shows that randomly placed particles tend to fill some of the gaps while also smoothing the distribution. And again, a higher number of particles tends to smooth the spectra, and the effect is even more noticeable on the spectra with low statistics, as shown in figure 18.

5.4.2. Final positions of the randomly placed particles

The simulations with 16.384 randomly placed particles still highlights over-densities and under-densities in the ejection maps. In addition, some structures where the particles have similar Lorentz factors still appear. In fact, figure 19 shows preferred directions for a given range of energy of particles.

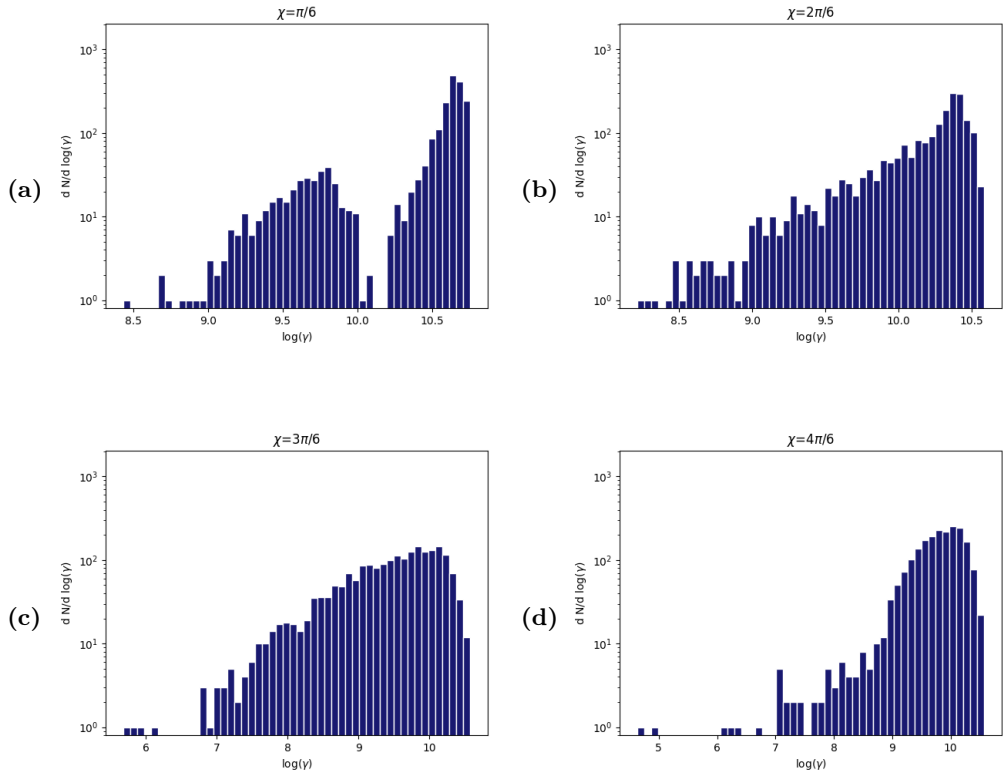


Figure 15: Comparison of the distribution functions for 2048 protons following the random placement: (a) inclination $\chi = 30^\circ$, (b) inclination $\chi = 60^\circ$, (c) inclination $\chi = 90^\circ$, (d) inclination $\chi = 120^\circ$.

In figure 20, impact positions are similar as in figure 14, still with gradients of energy depending of the position of impact. Interestingly, the hotspots for $\chi = 90^\circ$ are still crescent-shaped.

5.5. Aligned and anti-aligned neutron stars

A neutron star is aligned (respectively anti-aligned) when $\chi = 0^\circ$ (respectively $\chi = 180^\circ$). In these cases, it is easier to interpret the trajectories of particles. For protons near an aligned neutron star, the poles of the star are negatively charged while the equator is positively charged. This leads the protons to be pushed away from the equator and pulled by the poles. However, even if the magnetic field is strong enough, particles still reach the poles by following the field lines, allowing them to crash easily, and since as particles get closer to the surface the electric field gets more intense, they reach an even higher Lorentz factor as proven by the left spectrum (a) of figure 21.

Inversely, protons around an anti-aligned neutron stars will mostly be trapped around it since they are pulled toward the equator which is now negatively charged, but they cannot reach it due to the too strong magnetic field. These protons will feel an electric drift similar to that in figure 2 but this drift forces them to rotate around the neutron star, leading to a high spread in Lorentz factors on the right spectrum (b) of figure 21.

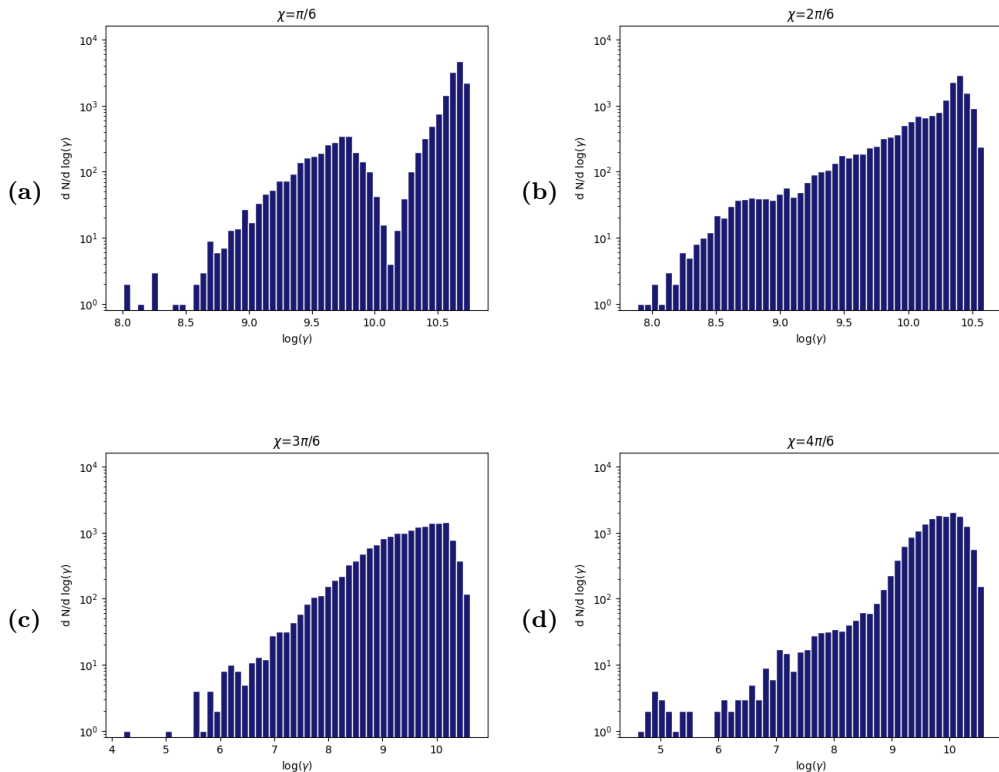


Figure 16: Comparison of the distribution functions for 16,384 protons following the random placement: (a) inclination $\chi = 30^\circ$, (b) inclination $\chi = 60^\circ$, (c) inclination $\chi = 90^\circ$, (d) inclination $\chi = 120^\circ$.

And with 16,384 randomly placed particles, the spectra appear to be more continuous and a peak not visible in figure 21 appears, as shown in figure 22, while keeping the same maximum Lorentz factor.

6. Conclusion

In this paper, we proved that our new algorithm to simulate particles acceleration in realistic ultra-strong neutron star electromagnetic fields is efficient and accurate. We put a constraint on the highest Lorentz factors that charged particles can reach thanks to our preliminary idealised model of a rotating magnet in vacuum.

Interestingly, the maximum Lorentz factors attainable by the particles scale linearly with their charge to mass ratio q/m . The code also retrieved two expected symmetries: a charge-latitude symmetry and a central symmetry relative to the centre of the pulsar. The inclination of the pulsar has an influence on the particle distribution functions and on their final positions. Actually, positive charges hit the surface of the neutron star only for $\chi \leq 90^\circ$.

This preliminary work is encouraging but still not straightforwardly applicable per se to real neutron stars electro-dynamics. Nevertheless, we will pursue our effort by studying

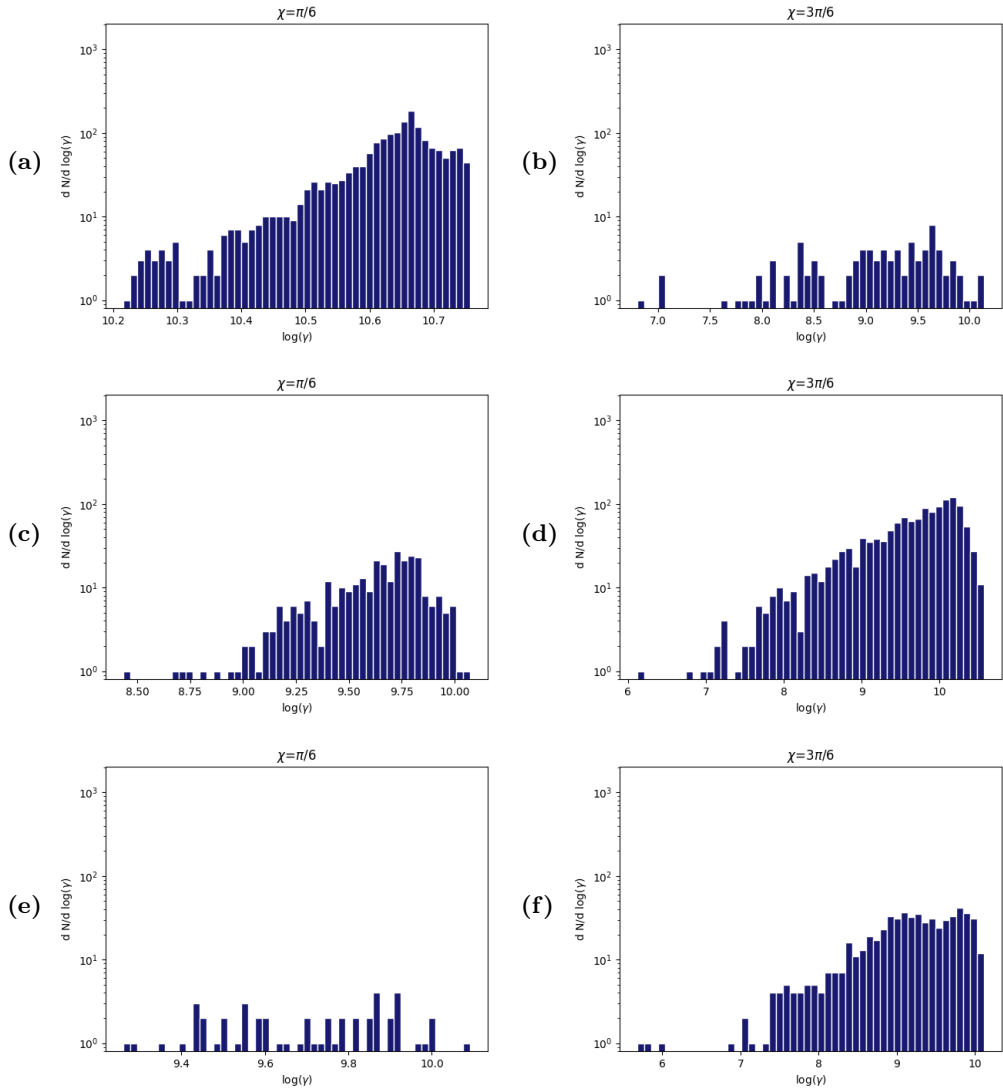


Figure 17: Protons distribution functions depending on their final state. (a) Crashed, $\chi = 30^\circ$, (b) Crashed, $\chi = 90^\circ$, (c) Ejected, $\chi = 30^\circ$, (d) Ejected, $\chi = 90^\circ$, (e) Trapped, $\chi = 30^\circ$, (f) Trapped, $\chi = 90^\circ$, for a random distribution of 2.048 particles.

the acceleration efficiency in a plasma filled magnetosphere, which is a more realistic case than the Deutsch vacuum field. Good starting points would be resistive magnetospheres (Li *et al.* 2012) as well as radiative magnetospheres (Pétri 2020*b,a*).

Because of the very high Lorentz factors, radiation reaction cannot be ignored as shown by Laue & Thielheim (1986). We plan to add this damped motion in an upcoming work. Our long standing goal is to inject particle due to pair creation and to implement the pusher into a particle in cell (PIC) or Vlasov code to fully and self-consistently simulate a pulsar magnetosphere with ultra-strong fields, generating current sheets and acceleration gaps. We expect a decrease of the Lorentz factors by several orders of magnitudes compared to the present investigation thanks to the screening of the field and the energy

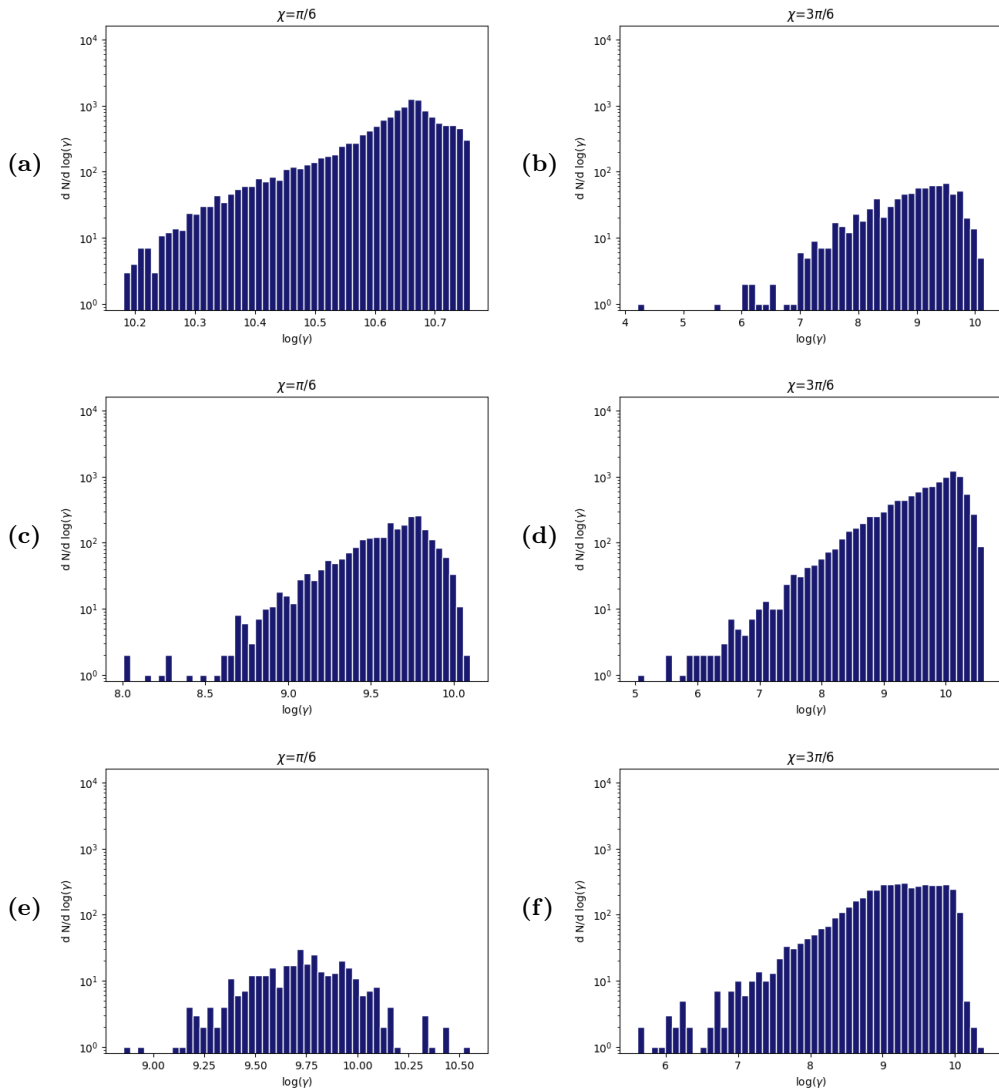


Figure 18: Protons distribution functions depending on their final state. (a) Crashed, $\chi = 30^\circ$, (b) Crashed, $\chi = 90^\circ$, (c) Ejected, $\chi = 30^\circ$, (d) Ejected, $\chi = 90^\circ$, (e) Trapped, $\chi = 30^\circ$, (f) Trapped, $\chi = 90^\circ$, for a random distribution of 16.384 particles.

lost via radiation. Our long lasting goal is to obtain kinetic solution of realistic pulsar magnetospheres. The feasibility of a PIC code implementing our analytical pusher has been shown by Pétri (2020c) who designed a 1D relativistic electromagnetic PIC code to simulate plasma oscillations, the relativistic two-stream instability and a strongly magnetized ultra-relativistic shock. We found there that the computational cost remains manageable, with only a small overhead compared for instance with the fully implicit scheme presented by Pétri (2017) and Vay (2008). The additional cost to boost particles and rotate the coordinate axes are largely compensated by the ability to compute realistic trajectories in ultra strong fields.

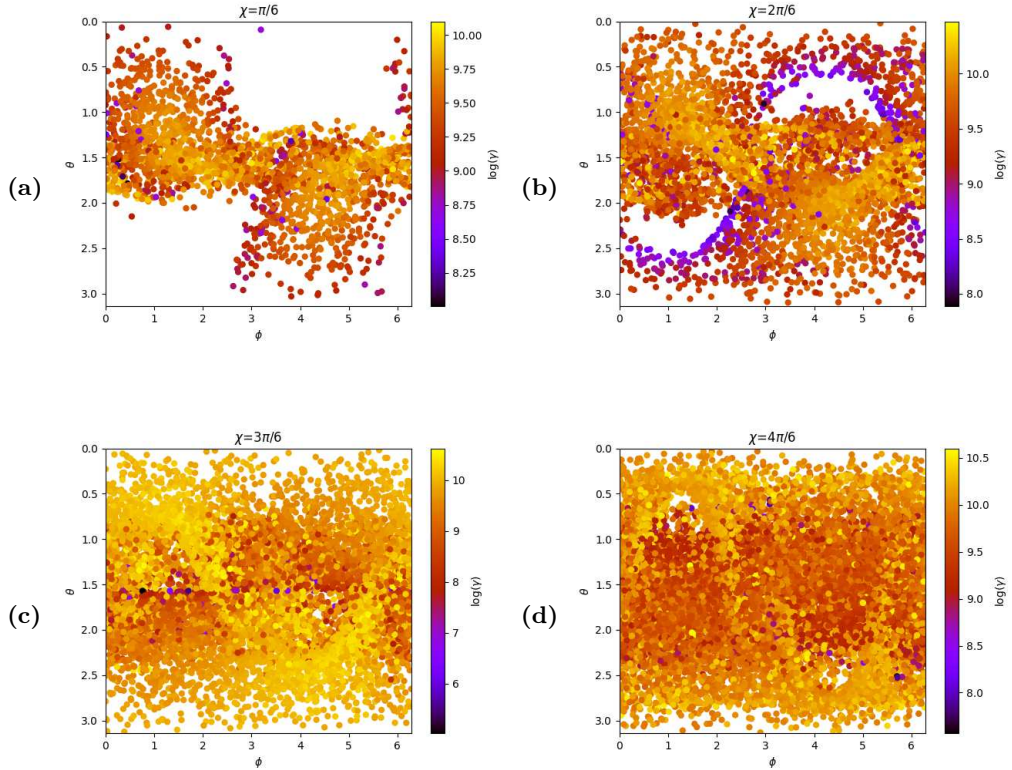


Figure 19: Ejection maps for 16.384 protons following the random placement: (a) inclination $\chi = 30^\circ$, (b) inclination $\chi = 60^\circ$, (c) inclination $\chi = 90^\circ$, (d) inclination $\chi = 120^\circ$.

Acknowledgement

We are grateful to the referees for helpful comments and suggestions. This work has been supported by CEFIPRA grant IFC/F5904-B/2018. We also acknowledge the High Performance Computing center of the University of Strasbourg for supporting this work by providing scientific support and access to computing resources. Part of the computing resources were funded by the Equipex Equip@Meso project (Programme Investissements d’Avenir) and the CPER Alsacalcul/Big Data.

REFERENCES

- AREFIEV, ALEXEY V., COCHRAN, GINEVRA E., SCHUMACHER, DOUGLASS W., ROBINSON, ALEXANDER P. L. & CHEN, GUANGYE 2015 Temporal resolution criterion for correctly simulating relativistic electron motion in a high-intensity laser field. *Phys. Plasmas* **22** (1), 013103.
- ARFKEN, GEORGE B. & WEBER, HANS-JURGEN 2005 *Mathematical methods for physicists*, 6th edn. Boston: Elsevier.
- BORIS, J.P. 1970 Relativistic plasma simulation-optimization of a hybrid code. *Proceeding of Fourth Conference on Numerical Simulations of Plasmas*.
- BRAMBILLA, GABRIELE, KALAPOTHARAKOS, CONSTANTINOS, TIMOKHIN, ANDREY N.,

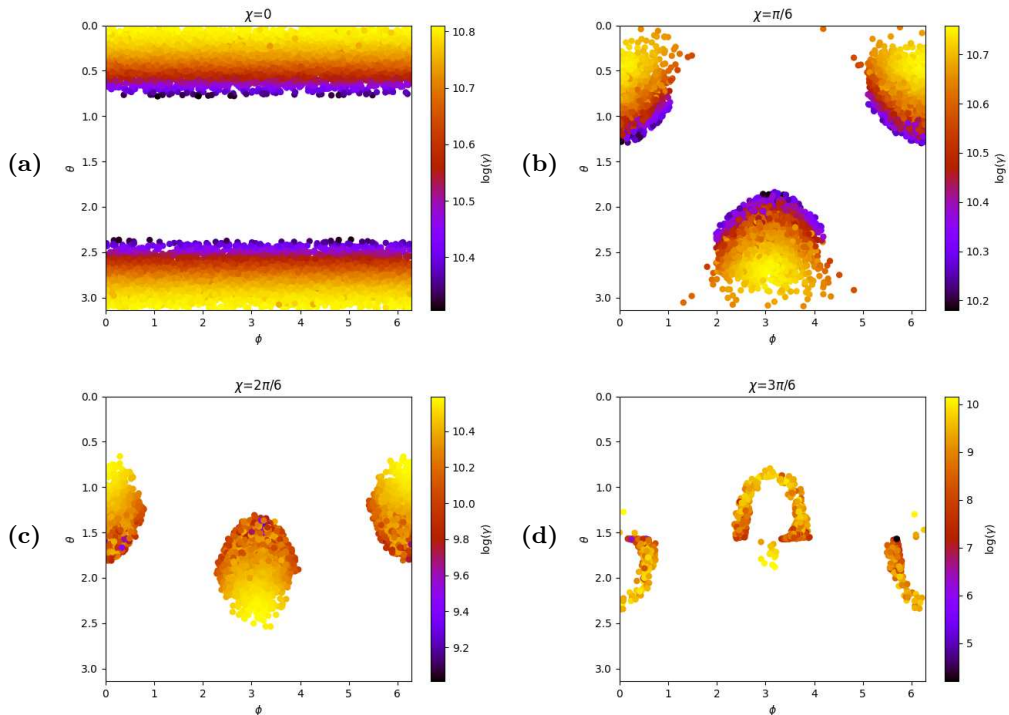


Figure 20: Impact maps of randomly placed protons on the neutron star surface for 16,384 particles, with $\chi = 0^\circ$ (a), $\chi = 30^\circ$ (b), $\chi = 60^\circ$ (c) and $\chi = 90^\circ$ (d).

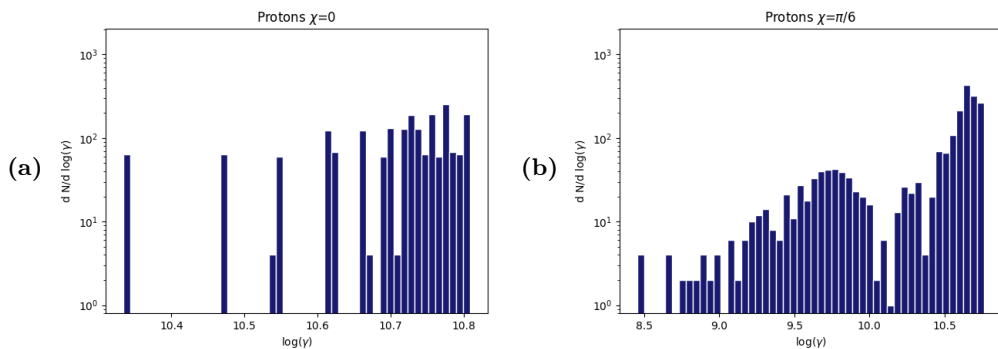


Figure 21: Spectra of protons in the aligned (a) and anti-aligned (b) cases, 2,048 protons placed on the regular pattern.

HARDING, ALICE K. & KAZANAS, DEMOSTHENES 2018 Electron-positron pair flow and current composition in the pulsar magnetosphere. *The Astrophysical Journal* **858** (2), 81, arXiv: 1710.03536.

CERUTTI, BENOÎT, PHILIPPOV, ALEXANDER, PARFREY, KYLE & SPITKOVSKY, ANATOLY 2015 Particle acceleration in axisymmetric pulsar current sheets. *MNRAS* **448**, 606–619.

DEUTSCH, ARNIM J. 1955 The electromagnetic field of an idealized star in rigid rotation in vacuo. *Annales d'Astrophysique* **18**, 1.

GOURGOLHON, ERIC 2010 *Relativité restreinte: Des particules à l'astrophysique*. EDP Sciences.

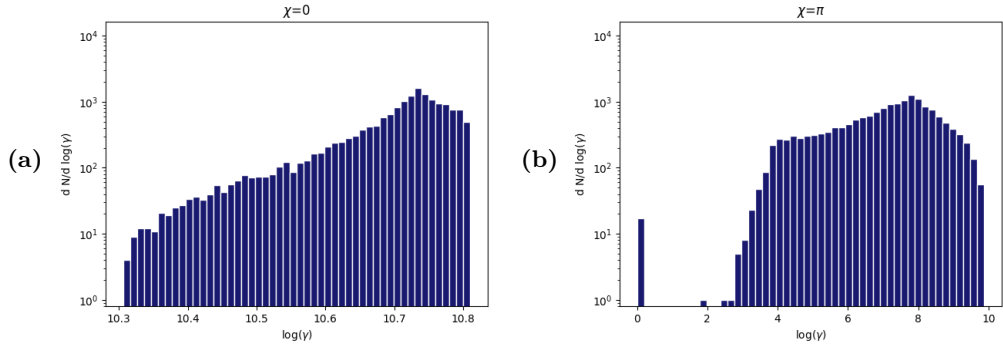


Figure 22: Spectra of 16,384 randomly placed protons in the aligned (a) and anti-aligned (b) cases.

- GUÉPIN, C., CERUTTI, B. & KOTERA, K. 2019 Proton acceleration in pulsar magnetospheres. *arXiv e-prints* p. arXiv:1910.11387, arXiv: 1910.11387.
- HIGUERA, ADAM V. & CARY, JOHN R. 2017 Structure-preserving second-order integration of relativistic charged particle trajectories in electromagnetic fields. *Physics of Plasmas* **24** (5), 052104, arXiv: 1701.05605.
- KALAPOTHARAKOS, KONSTANTINOS, BRAMBILLA, GABRIELE, TIMOKHIN, ANDREY, HARDING, ALICE K. & KAZANAS, DEMOSTHENES 2018 Three-dimensional Kinetic Pulsar Magnetosphere Models: Connecting to Gamma-Ray Observations. *The Astrophysical Journal* **857** (1), 44, arXiv: 1710.03170.
- KRAUSE-POLSTORFF, J. & MICHEL, F. C. 1985 Electrosphere of an aligned magnetized neutron star. *Monthly Notices of the Royal Astronomical Society* **213**, 43P–49P.
- LAPENTA, GIOVANNI & MARKIDIS, STEFANO 2011 Particle acceleration and energy conservation in particle in cell simulations. *Physics of Plasmas (1994-present)* **18** (7), 072101.
- LAUE, H. & THIELHEIM, K. O. 1986 Acceleration of protons and electrons in the electromagnetic field of a rotating orthogonal magnetic dipole. *The Astrophysical Journal Supplement Series* **61**, 465–478.
- LI, JASON, SPITKOVSKY, ANATOLY & TCHEKHOVSKOY, ALEXANDER 2012 Resistive Solutions for Pulsar Magnetospheres. *ApJ* **746** (1), 60.
- MICHEL, F. C. & LI, H. 1999 Electrodynamics of neutron stars. *Physics Reports* **318** (6), 227–297.
- PHILIPPOV, ALEXANDER A. & SPITKOVSKY, ANATOLY 2014 Ab Initio Pulsar Magnetosphere: Three-dimensional Particle-in-cell Simulations of Axisymmetric Pulsars. *The Astrophysical Journal Letters* **785** (2), L33, arXiv: 1312.4970.
- PÉTRI, J. 2017 A fully implicit scheme for numerical integration of the relativistic particle equation of motion. *J. Pl. Ph.* **83** (02), arXiv: 1612.04563.
- PÉTRI, JÉRÔME 2020a Electrodynamics and Radiation from Rotating Neutron Star Magnetospheres. *MNRAS* **6** (1), 15.
- PÉTRI, J. 2020b Radiative pulsar magnetospheres: aligned rotator. *MNRAS* **491**, L46–L50.
- PÉTRI, J. 2020c A relativistic particle pusher for ultra-strong electromagnetic fields. *ArXiv e-prints* (arXiv: 1910.04591), arXiv: 1910.04591.
- PÉTRI, J., HEYVAERTS, J. & BONAZZOLA, S. 2002 Global static electrospheres of charged pulsars. *A&A* **384**, 414–432.
- QIN, HONG, ZHANG, SHUANGXI, XIAO, JIANYUAN, LIU, JIAN, SUN, YAJUAN & TANG, WILLIAM M. 2013 Why is Boris algorithm so good? *Physics of Plasmas* **20** (8), 084503.
- RIPPERDA, B., BACCHINI, F., TEUNISSEN, J., XIA, C., PORTH, O., SIRONI, L., LAPENTA, G. & KEPPENS, R. 2018 A Comprehensive Comparison of Relativistic Particle Integrators. *ApJS* **235** (1), 21.
- UMEDA, TAKAYUKI 2018 A three-step Boris integrator for Lorentz force equation of charged particles. *Computer Physics Communications* **228**, 1–4.

- UZAN, JEAN-PHILIPPE & DERUELLE, NATHALIE 2014 *Théories de la Relativité*. Paris: Belin.
- VAY, J.-L. 2008 Simulation of beams or plasmas crossing at relativistic velocity. *Physics of Plasmas (1994-present)* **15** (5), 056701.
- VERBONCOEUR, J. P. 2005 Particle simulation of plasmas: review and advances. *Plasma Phys. Control. Fusion* **47** (5A), A231.
- VRANIC, M., MARTINS, J. L., FONSECA, R. A. & SILVA, L. O. 2016 Classical radiation reaction in particle-in-cell simulations. *Computer Physics Communications* **204**, 141–151.
- ZENITANI, SEIJI & UMEDA, TAKAYUKI 2018 On the Boris solver in particle-in-cell simulation. *arXiv:1809.04378 [physics]* ArXiv: 1809.04378.
- ZHANG, RUILI, LIU, JIAN, QIN, HONG, WANG, YULEI, HE, YANG & SUN, YAJUAN 2015 Volume-preserving algorithm for secular relativistic dynamics of charged particles. *Physics of Plasmas* **22** (4), 044501.